World Scientific
www.worldscientific.com

Supercontinuum generation in $C_6H_5NO_2$-core photonic crystal fibers with various air-hole size

Trong Dang Van[*] and Lanh Chu Van[†]

Department of Physics, Vinh University,
182 Le Duan, Vinh City 43100, Viet Nam
[*]dangvantrong0602@gmail.com
[†]chuvanlanh@vinhuni.edu.vn

In this paper, we demonstrated the ability of a hexagonal photonic crystal fiber (PCF) with a hollow core infiltrated with nitrobenzene ($C_6H_5NO_2$) to generate a broad SC spectrum at low peak powers. Due to the non-uniformity of the air hole diameters, our new design allows for simultaneous optimization of features, resulting in near-flat, near-zero dispersion, a small effective mode area, and low attenuation for efficient spectral broadening. We selected two optimal structures from the simulation results to analyze the nonlinear properties and supercontinuum generation. The first fiber, #HF_1, with a lattice constant of $1.0\,\mu m$ and a filling factor of 0.45, operates in all-normal dispersion and produces spectral SC ranging from $0.81\,\mu m$ to $1.919\,\mu m$ with a pump wavelength of $1.56\,\mu m$, a pulse duration of 90 fs, and peak power of $0.133\,kW$ propagated in a 1 cm fiber length. The #HF_2 fiber (lattice constant of $2.0\,\mu m$, filling factor of 0.3) has an extended SC spectrum from $0.792\,\mu m$ to $3.994\,\mu m$, a pump wavelength of $1.55\,\mu m$, a pulse width of 110 fs, a peak power of $0.273\,kW$ propagated in a 15 cm fiber length. The proposed fiber may be a new-generation optical fiber suitable for low-peak power all-fiber optical systems to replace glass-core glass fiber.

Keywords: Photonic crystal fiber (PCF); nitrobenzene-core ($C_6H_5NO_2$-core); hexagonal lattice; supercontinuum generation; all-normal dispersion; anomalous dispersion.

1. Introduction

Supercontinuum generation (SCG) is the process of generating a broadband optical spectrum by injecting an optical pulse into a nonlinear medium, where the continuous interaction of the laser pulse with the nonlinear optical medium increases the bandwidth by many times. A broader light spectrum is emitted and larger than the original pulse. SCG was first described by Alfano and Shapiro in 1970.[1] Some interesting applications of SCG are spectroscopy, optical microscopy, optical communication, security, military, optical coherent tomography, biomedicine,

[†]Corresponding author.

frequency comb generation, and nonlinear optical pulse compression.[2–6] SCG derives from nonlinear processes such as self-phase modulation (SPM), optical wave breaking (OWB), cross-phase modulation (XPM), Stimulated Raman scattering (SRS), Raman-Kerr scattering (RKS), modulation instability (MI), soliton fission (SF), soliton self-frequency shift (SSFS), and dispersive wave (DW).[7–9]

The object most effectively used for SCG is a photonic crystal fiber (PCF). With high nonlinearity and tunable dispersion characteristics that can produce broad and smooth SC spectra, a special design of his PCF that achieves flat dispersion and high nonlinear loading depending on the pump parameters is required. In addition, properties such as dispersion, effective mode area, and attenuation are also factors that affect SCG performance. The flat dispersion, low loss, and small effective mode area of the PCF result in the best-performing SCG. By designing and tuning the structural parameters of PCFs, such as lattice constant, air hole size, shape, solid or hollow core, and materials, the optimal properties of PCFs can be obtained.

Several years ago, silica-based solid-core PCFs were suitable for near-infrared (near-IR) and visible SC generation. However, silica (SiO_2) has a low nonlinear refractive index and high mid-infrared (m-IR) attenuation, so the spectrum cannot exceed $2.5\,\mu$m. On the other hand, solid-core PCFs and soft-glass PCFs can overcome spectral broadening limitations compared to silica PCFs, but are limited in terms of manufacturing technology, complex pumping systems, and high costs.[10–12] Therefore, recently, the investigated liquid-filled hollow core has been discussed in several papers.[13–30] PCF using low-energy pump pulses in short-fiber samples SC with spectral width from visible to m-IR.[13–30] It outperforms silica and many other soft glasses in enhancing the nonlinearity of PCF. According to this method, liquids with a high nonlinear refractive index such as carbon disulfide (CS_2),[17,18] carbon tetrachloride (CCl_4),[19–21] chloroform ($CHCl_3$),[22] nitrobenzene ($C_6H_5NO_2$),[13,23,24] benzene (C_6H_6),[25] tetrachloroethylene (C_2Cl_4),[26,27] 1–2 dibromoethane ($C_2H_4Br_2$),[28] and toluene (C_7H_8)[29,30] were used injected into the core of the PCF with a Silica substrate to obtain a broad and coherent SC spectrum. The results show that by varying the temperature and pressure of the PCF, the SC spectra can be controlled and acquired in both perfectly normal and anomalous dispersion regions. However, PCF in the above analysis has the same air hole size in the photonic cladding, so only dispersion can be optimized, but not effective mode area and loss. So SCG performance is still limited.

The authors in Ref. 31 proved that the first lattice ring directly affects the dispersion properties, including zero-dispersion flatness and wavelength shift, while the remaining lattice rings affect the loss and effective mode area. Figure 1(a) shows a cross-section of the PCF structure in Ref. 31, but in this work, the author only analyzed the characteristic quantities of the solid-core PCF structure and not its application to SCG.

To overcome the above limitations, we developed a new hollow-core PCF filled with nitrobenzene with a hexagonal lattice. In this paper, we present for the first time the possibility of achieving a wide SC spectrum using very low peak power for PCF with near-zero flat dispersion. The difference between the air-hole diameters of the
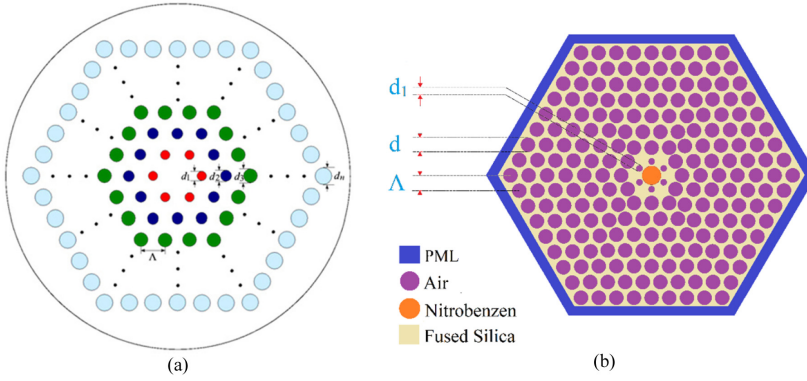
Fig. 1.   (Color online) The geometrical structure of PCF: (a) PCF in Ref. 31 and (b) PCF in our work.

first ring and the air-hole diameters of the remaining rings is the highlight of this work. Structural parameters of PCFs, such as filling factor (d_1/Λ) and lattice constant (Λ), are controlled to obtain optimal structures that are assumed to have near-zero flat dispersion, small effective mode area, high nonlinear coefficients, and loss considered as zero. We perform SC generation with optimized fibers and achieve greater bandwidth than previous works with low peak power.

2. Numerical Modeling of PCF

In this study, the finite element method (FDE), which is widely used for optical fiber analysis, is used to design and optimize the fiber structure. Numerical analysis was performed using the Lumerical Mode Solution software.[32] A cross-section of the proposed PCF is shown in Fig. 1(b). The PCF has a standard hexagonal shape, with a ring of eight air holes surrounding an empty core filled with nitrobenzene ($C_6H_5NO_2$-core) within a fused silica cladding. We emphasize the choice of nitrobenzene to fill the hollow-core PCF due to its high nonlinear refractive index of $n_2 = 671 \times 10^{-20}\,\mathrm{m^2\,W^{-1}}$ at $1064\,\mathrm{nm}$.[33] This value of nitrobenzene is about 240 times higher than that of silica[28] and higher than that of other liquids such as $CHCl_3$,[22] CCl_4,[19–21] C_2Cl_4,[26,27] C_7H_8.[29,30] $C_6H_5NO_2$ is a water-insoluble pale yellow oil with a specific odor of almonds. $C_6H_5NO_2$ enters the core by integrating micro-fluidic injection systems using fusion splicers[30] or laser scribing techniques.[34] Figure 2[35] shows the visible and near-infrared transmission spectra of a $9.8\,\mathrm{mm}$ thick cuvette filled with $C_6H_5NO_2$. $C_6H_5NO_2$ has a strong absorption at wavelengths above $1600\,\mathrm{nm}$, but is transparent over the entire visible range and between $1200\,\mathrm{nm}$ and $1600\,\mathrm{nm}$. The material attenuation of $C_6H_5NO_2$ in the visible wavelength range and the near-IR that was experimentally measured by us are shown in Fig. 3.

We designed a PCF structure with different diameters of the air holes in the first ring and the rest of the rings. The diameter of the air holes in the first ring (the inner ring closer to the core) is d_1, which corresponds to a filling factor of d_1/Λ. In contrast, the diameter of the air holes in the remaining lattice rings is d, corresponding to the
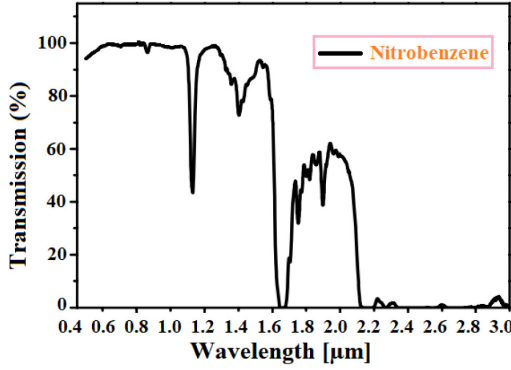
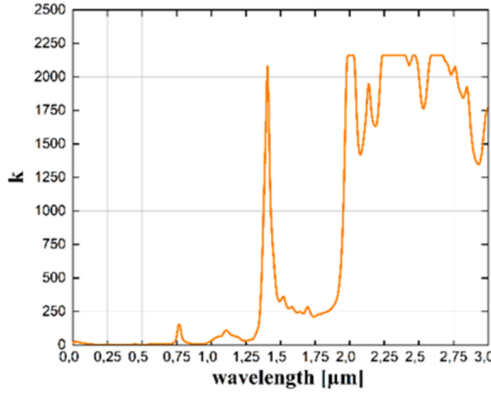Fig. 2.   (Color online) The transmission curves of a 9.8 mm thick cuvette of $C_6H_5NO_2$.[29]

Fig. 3.   (Color online) The imaginary part of the refractive index k of $C_6H_5NO_2$.

filling factor d/Λ. We control the filling factor d_1/Λ to optimize the dispersion properties and set the filling factor (d/Λ) of the remaining lattice rings to 0.95 to optimize the effective mode area and loss. The lattice constant (Λ) chosen for this study varies from $1.0\,\mu m$ to $2.5\,\mu m$ with a step size of $0.5\,\mu m$ and the filling factor d_1/Λ varies from 0.3 to 0.8 with a step size of 0.05. The diameter of the core (D_c) depends on d_1 and the lattice constant (Λ) and is determined by $D_c = 2\Lambda - 1.1d_1$.

The linear properties of the PCF, including dispersion, effective mode area, and attenuation, are computed based on the "Full Vector Finite Difference Mode Solver".[36] In this solver, the fiber cross-section is divided into small rectangular sections called "Yee's mesh". The optical properties of each Yee mesh are approximated as unchanged. For points lying on the surface between two media, an index averaging technique is used for cells across the interface. Optimization algorithms may lead to better optical properties, but we do not use optimization algorithms. The structural parameters of the PCF are very small consistent with the "stack-and-draw" manufacturing process of about $50\,nm$[37] (e.g. the fill factor changes by 0.05 and the lattice constant changes around 0.5 microns). Moreover, using optimization

Table 1. Sellmeier's coefficients of the material used.

	Sellmeier's coefficients					
Material	A_1	A_2	A_3	B_1 [μm^2]	B_2 [μm^2]	B_3 [μm^2]
SiO$_2$	0.6694226	0.4345839	0.8716947	4.4801×10^{-3}	1.3285×10^{-2}	95.341482
C$_6$H$_5$NO$_2$	1.30628	0.00502	—	0.02268	0.18487	—
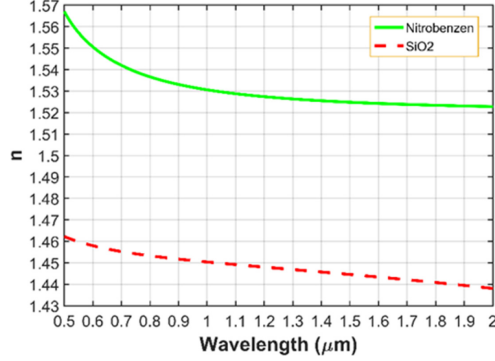
Fig. 4. (Color online) Real parts of the refractive index of C$_6$H$_5$NO$_2$ and SiO$_2$.

algorithms during simulation takes a lot of time. Therefore, a simpler method based on the optimization of dispersion properties was applied.

The real part of the linear refractive index n of C$_6$H$_5$NO$_2$[38] and SiO$_2$[39] is calculated as a function of wavelength using the Sellmeier formula in the following equation:

$$n(\lambda) = \sqrt{1 + \frac{A_1\lambda^2}{\lambda^2 - B_1} + \frac{A_2\lambda^2}{\lambda^2 - B_2} + \frac{A_3\lambda^2}{\lambda^2 - B_3}}. \tag{1}$$

Values of the Sellmeier's coefficients $A_1, \ldots, A_3$, and $B_1, \ldots, B_3$ are listed in Table 1 and λ is the wavelength of light in μm.

Figure 4 shows the real part characteristic of the wavelength refractive index of C$_6$H$_5$NO$_2$ compared with that of fused silica. It can be seen that the refractive index of C$_6$H$_5$NO$_2$ and SiO$_2$ varies linearly with each other, and the refractive index of C$_6$H$_5$NO$_2$ is always greater than that of SiO$_2$. Light transmitted in silica-based PCFs with a C$_6$H$_5$NO$_2$-core follows the same total internal reflection mechanism as that of conventional optical fibers.

3. Optimization of the Characteristic Quantities of PCF

We present the fundamental mode dispersion. Chromatic dispersion (D) of a PCF includes both the material dispersion and the waveguide dispersion and can be defined by using the following equation[40]:

$$D = -\frac{\lambda}{c} \frac{\partial^2 \text{Re}[n_{\text{eff}}]}{\partial \lambda^2}, \tag{2}$$

where $\text{Re}[n_{\text{eff}}]$ is the real part of n_{eff} which is the effective index of the guided mode calculated using the FDE method and c is the speed of light in a vacuum.

The nonlinear coefficient of PCF has the unit of $(\text{W}^{-1} \cdot \text{km}^{-1})$ determined by the formula in the following equation[40]:

$$\gamma = \frac{\omega}{c}\left(\frac{n_2}{A_{\text{eff}}}\right) = \frac{2\pi}{\lambda}\left(\frac{n_2}{A_{\text{eff}}}\right), \tag{3}$$

where ω is the angular frequency, and A_{eff} is the effective mode area (an important characteristic of PCF). It is inversely proportional to the nonlinear coefficient and is defined as in the following equation[40]:

$$A_{\text{eff}} = \frac{(\int_{-\infty}^{\infty}\int_{-\infty}^{\infty}|E(x,y)|^2 dxdy)^2}{\int_{-\infty}^{\infty}\int_{-\infty}^{\infty}|E(x,y)|^4 dxdy}, \tag{4}$$

where E is the electric field amplitude.

Figure 5 shows the effect of varying the filling factor (d_1/Λ) and lattice constant (Λ) on the dispersion (D). Looking at the diagram, we can see that the dispersion of
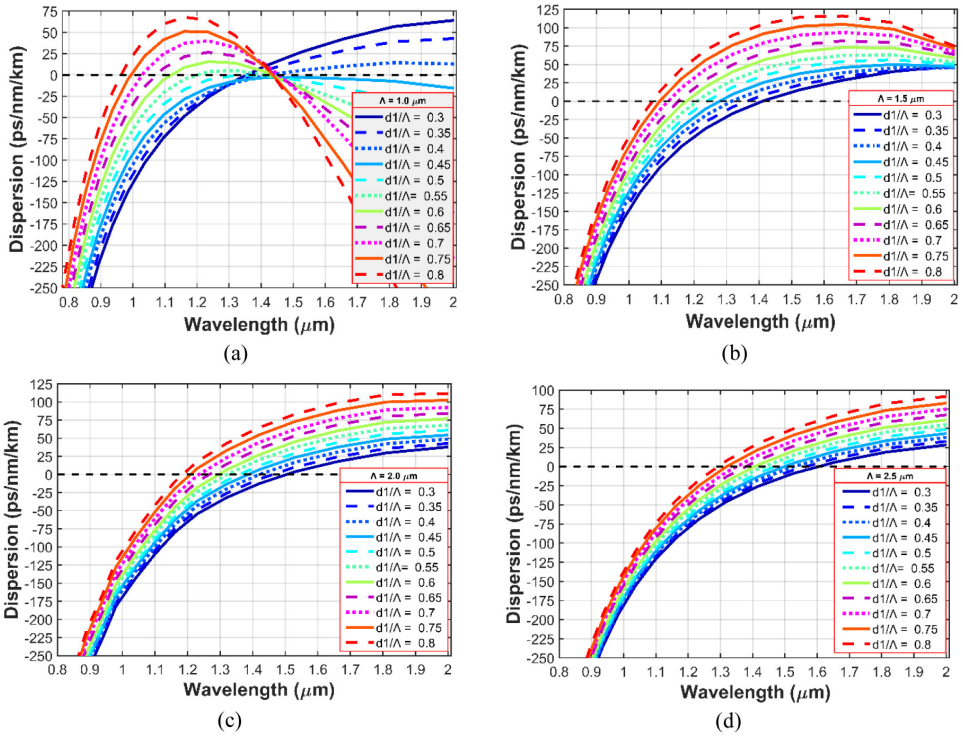

Fig. 5. (Color online) Characteristics of chromatic dispersion of the fundamental mode for PCFs infiltrated nitrobenzene with hexagonal lattice with (a) $1.0\,\mu\text{m}$, (b) $1.5\,\mu\text{m}$, (c) $2.0\,\mu\text{m}$, and (d) $2.5\,\mu\text{m}$. d_1/Λ varies from 0.3 to 0.8.

the hexagonal lattice structure varies with wavelength. The resulting dispersion curves contain perfectly normal and anomalous dispersions with one or two ZDWs. The dispersion properties were governed by changing the filling factor d_1/Λ and the lattice constant (Λ). Moreover, changing these two parameters shifts the ZDW to longer wavelengths. When the lattice constant is small ($\Lambda = 1.0\,\mu$m, Fig. 5(a), the PCF exhibits both anomalous and all-normal dispersion properties. A PCF with two ZDW values can be obtained for $0.5 \leq d_1/\Lambda \leq 0.8$, whereas a PCF with only one ZDW is obtained with a smaller d_1/Λ (0.3–0.4) in the examined wavelength range. In this case, the all-normal dispersion regime occurs only when $d_1/\Lambda = 0.45$. This fiber has flat dispersion and a near-zero dispersion curve in the long wavelength range, which should be useful for SC generation. On the other hand, all PCFs with larger cores ($\Lambda = 1.5\,\mu$m, $\Lambda = 2.0\,\mu$m, $\Lambda = 2.5\,\mu$m) are in the anomalous dispersion region with one ZDW. Moreover, for a given value of Λ ($\Lambda > 1.0\,\mu$m), the ZDW shifts to longer wavelengths as the filling factor d_1/Λ decreases. In contrast, for some values of fill factor d_1/Λ, the ZDW shifts to shorter wavelengths as Λ decreases. The above analysis and simulation results show that by carefully tuning the air hole diameter d_1 of the first ring of the PCF structure, it seems that the desired dispersion properties of the structure can be easily obtained.

To obtain an SCG with a broad and flat spectrum, we need to find a PCF structure with near-zero flat dispersion and ZDW compatibility with the pump wavelength. By controlling structural parameters to achieve optimal dispersion, we propose two optimal PCFs, namely #HF₁ and #HF₂ that are beneficial for SC generation. Both introduced PCF structures have reasonably flat dispersion and near-zero dispersion curves in the investigated wavelength range, as shown in Fig. 6(a). Structural parameters of the fibers are shown in Table 2.

The first fiber #HF₁ was used for SG in the all-normal dispersion regime with a pump wavelength of $1.56\,\mu$m to obtain the broadest SC spectrum, because the pump wavelength is close to the maximum dispersion value. The second #HF₂ fiber has an anomalous dispersion regime, but is expected to produce a broad-spectrum SC at a pump wavelength of $1.55\,\mu$m, as its ZDW is closest to the pump wavelength at $1.502\,\mu$m. The dispersions of #HF₁ and #HF₂ fibers at the pump wavelength are $-3.18\,\text{ps} \cdot \text{nm}^{-1} \cdot \text{km}^{-1}$ and $6.215\,\text{ps} \cdot \text{nm}^{-1} \cdot \text{km}^{-1}$, respectively.

Figure 6(b) shows the fundamental mode attenuation characteristics of #HF₁ and #HF₂ fibers. The attenuation of #HF₁ and #HF₂ fibers tended to be similar in the investigated wavelength range. The attenuation value at 1.56 pump wavelength for #HF₁ fiber is $6.25\,\text{dB/cm}$, which corresponds to $4.92\,\text{dB/cm}$ for #HF₂ at $1.55\,\mu$m. Low attenuation is an advantage of our model compared to previous studies. The reason for the low value of attenuation for the fundamental mode of our design is that the mode is well confined in the core; the majority of the electromagnetic field is located there and the losses introduced by toluene are not mostly affected. The effective mode area of the proposed PCF is shown in Fig. 6(c). The results in the figure show that the effective mode area for both fibers increases linearly with increasing wavelength. As the wavelength increases, the light is no
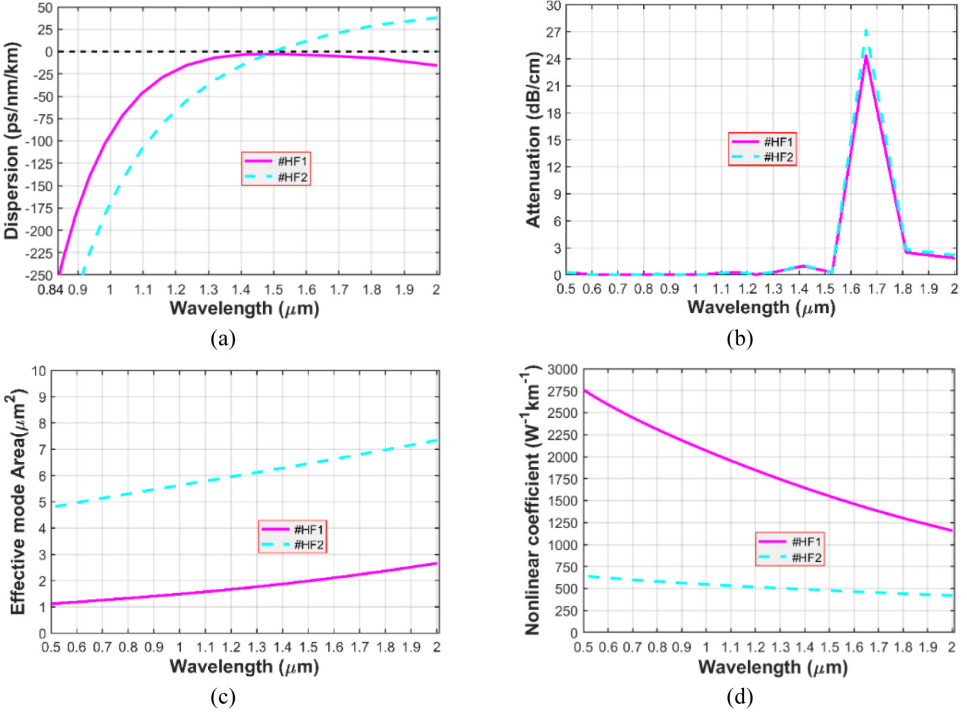
Fig. 6. (Color online) The characteristics of the fundamental mode for #HF$_1$ and HF$_2$. (a) dispersion, (b) attenuation, (c) effective mode area, and (d) nonlinear coefficient.

Table 2. The structure parameters of proposed PCFs.

Parameter	#HF$_1$	#HF$_2$
Lattice pitch Λ [μm]	1.0	2.0
Filling factor d_1/Λ	0.45	0.3
Core diameter D_c [μm]	1.505	3.34

longer confined strongly inside the core because the modes get leaked through the holes, in between them increasing the effective mode area. Due to the larger core diameter, the effective mode area for #HF$_2$ is always larger than that of #HF$_1$ fiber. At the pump wavelength, the effective mode area values for fibers #HF$_1$ and #HF$_2$ are 2.059 (μm^2) and 6.538 (μm^2), respectively. The nonlinear coefficient is inversely proportional to the effective mode area according to Eq. (3), so the nonlinear coefficient of the fibers rises along with the decrease of the effective mode area, Fig. 6(d). As expected, the alteration of the filling factor and the lattice constant significantly improves the nonlinearity coefficient of fibers. The nonlinearity of fiber #HF$_1$ is always larger than that of #HF$_2$, the nonlinearity value of the former is 1497 (W^{-1}· km^{-1}) at the pump wavelength, while the nonlinearity of #HF$_2$ is 471 (W^{-1} · km^{-1}).

Table 3. The characteristic quantities values of the proposed PCFs in comparison with previous publications.

#	Pump wavelength (μm)	D (ps/nm $\cdot$ km)	A_{eff} (μm^2)	γ (km$^{-1}\cdot$W^{-1})	Attenuation (dB/cm)	Regime
#HF$_1$	1.56	-3.18	2.059	1496	6.25	All-normal
#HF$_2$	1.55	6.215	6.538	471	4.92	Anomalous
CCl$_4$[21]	1.03	-85	42.2	22.1	—	All-normal
C$_2$Cl$_4$, #F$_1$[26]	1.56	-15.0	433.2	156.9	0.04	All-normal
C$_2$Cl$_4$, #F$_2$[26]	1.56	3.20	16.67	40.79	0.042	Anomalous
C$_2$Cl$_4$, #F$_3$[26]	1.03	-4.85	359.1	189.3	0.053	Anomalous
C$_7$H$_8$, #I_0.3[29]	1.55	-7.784	7.79	1200	0.4	All-normal
C$_7$H$_8$, #I_0.35[29]	1.55	-1.19	78.9	—	1.2	Anomalous
C$_7$H$_8$[30]	1.03	$-150 \div -5$	73.2	130	—	All-normal

Table 3 shows a comparison between the proposed fiber properties and previously published values.

4. Supercontinuum Generation in Selected Fibers

We performed numerical simulations of SC generation for the two proposed fibers #HF$_1$ and #HF$_2$. In our simulations, the laser pulses used in the simulation were modeled by Gaussian pulses centered at the pump wavelength with P_0 as peak power, t_0 as pulse duration, and displayed in the following equation[41]:

$$A(T) = \sqrt{P_0}\exp\left(\frac{-T^2}{2t_0^2}\right). \tag{5}$$

The nonlinear propagation process of the pump pulse in the PCF can be expressed in terms of the Schrödinger equation (GNLSE) using the symmetric split-step Fourier transform method,[37] which is given by the following formula:

$$\partial_z\tilde{A} - i\tilde{\beta}(\omega)\tilde{A} - \frac{\tilde{\alpha}(\omega)}{2}\tilde{A} = i\gamma\left(1 + \frac{\omega - \omega_0}{\omega_0}\right)\tilde{A}F\left[\int_{-\infty}^{\infty} R(T')|A|^2(T - T')dT'\right], \tag{6}$$

where $\tilde{A}(z,\omega)$ is Fourier transform of the amplitude of a pulse $A(t)$, and $R(T')$ is the Raman response function. The nonlinear material response function $R(T)$ is described by a function representing two decaying harmonic oscillators with the main contributions from the electronic-bound and the nuclear parts, assuming that the electronic factor is the mechanism described by[37]

$$R(T) = (1 - f_R)\delta(T) + f_R h_R(T), \tag{7}$$

where $\delta(T)$ is the Dirac delta function and $h_R(T)$ is the delayed response. f_R is a part of the delayed contribution, which is a fraction of the nuclear contribution to the nonlinear optical response of nitrobenzene. The delay characteristics of the nonlinear response are comparable to Raman-induced frequency shifts. Energy moves to longer wavelengths with redshift. Therefore, we can find the partial contribution of delayed

Raman to the total nonlinear response after normaliza $h_R(T)$.[37]

$$h_R(T) = \frac{\tau_1^2 + \tau_2^2}{\tau_1^2 \tau_2^2} \exp\left(\frac{-T}{\tau_1}\right) \sin\left(\frac{T}{\tau_2}\right) \Theta(T), \tag{8}$$

where $\Theta(T)$ is the Heaviside step function, τ_1 and τ_2 correspond, respectively, to the inverse of the phonon oscillation frequency and the bandwidth of the Raman gain spectrum.

On the left side of Eq. (6), the linear parameters α and β represent propagation loss and dispersion in the frequency domain of the optical fiber, respectively. The higher-order dispersion shows its important influence as the input pulse's center wavelength approaches ZDW and is computed through the development coefficients of the Taylor series around the center wavelength ω_0, the expansion of the propagation constant (β) can be obtained by[42]

$$\beta_k(\omega) = \left.\frac{d^k \beta(\omega)}{d\omega^k}\right|_{\omega=\omega_0}, \tag{9}$$

where $k = 2, 3, 4, \ldots$ is the dispersion coefficient. The high-order dispersions at the pumping pulse frequency in our numerical modeling are displayed in Table 4.

In this section, we study in detail how dispersion and nonlinear properties can affect the generation of quality SC spectra for the proposed fiber #HF$_1$ and #HF$_2$. For #HF$_1$ fiber, the SC generation in the all-normal dispersion regime is pumped at $1.56\,\mu m$, the pulse duration is 90 fs, and the peak power varies from 0.022 kW to 0.133 kW (corresponding to input pulse energy from 0.002 nJ to 0.012 nJ). The pulse propagation length for the #HF$_1$ fiber is 1 cm. While #HF$_2$ fiber has anomalous dispersion properties with one ZDW at $1.502\,\mu m$ wavelength and the SC generation was analyzed with peak power ranging from 0.009 kW to 0.273 kW (corresponding to pulse energies from 0.001 nJ to 0.03 nJ, respectively) at a propagation length of 15 cm, a pump wavelength of $1.55\,\mu m$, and a pulse duration of 110 fs.

Figure 7(a) depicts the spectral broadening according to various peak power in the 1 cm #HF$_1$ fiber sample. The SC generation process is very fast and occurs in the

Table 4. The coefficient of high-order dispersion at the pump wavelength.

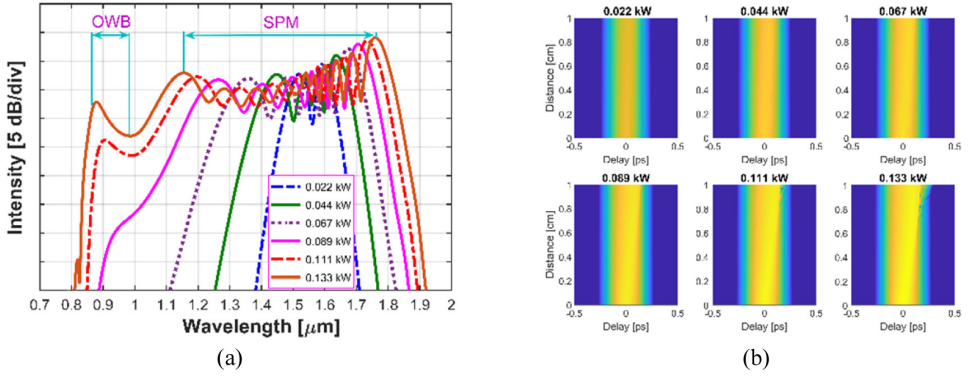| Coefficient	#HF$_1$	#HF$_2$
β_2 (ps^2/m)	3.99×10^{-3}	-7.44×10^{-3}
β_3 (ps^3/m)	-2.11×10^{-5}	2.40×10^{-4}
β_4 (ps^4/m)	2.34×10^{-7}	-2.92×10^{-7}
β_5 (ps^5/m)	7.01×10^{-10}	-9.37×10^{-9}
β_6 (ps^6/m)	3.25×10^{-11}	-2.44×10^{-11}
β_7 (ps^7/m)	-6.61×10^{-13}	3.59×10^{-12}
β_8 (ps^8/m)	2.68×10^{-15}	-1.33×10^{-16}
β_9 (ps^9/m)	-1.75×10^{-17}	-1.21×10^{-15}
β_{10} (ps^{10}/m)	6.48×10^{-19}	6.60×10^{-18}
β_{11} (ps^{11}/m)	3.93×10^{-20}	2.99×10^{-19}

Fig. 7.   (Color online) For #HF$_1$ fiber: (a) the output spectrum for various peak power pulses when using pump pulses with 1.56 μm pump wavelength and 90 fs duration and (b) the temporal profile at different positions of the propagation length, respectively, with the spectrum growing along the fiber.

first millimeter of the fiber due to the high nonlinearity of $C_6H_5NO_2$. Dispersion, SPM, and OWB effects are mainly responsible for the process of the SC generation process because the pump pulse works in the normal dispersion region of the #HF$_1$ fiber. It can be seen that the spectral width increases as the peak power increases, and the spectrum width also increases. For pump fibers with powers below less than 0.089 kW, SPM makes the greatest contribution to spectral broadening. This limits the spectrum to contain many peaks, with the outermost peaks having the strongest intensity. When the peak power is greater than 0.089 kW, the SC spectrum is determined by the SPM early stage of propagation and the resulting spectrum becomes asymmetric for short wavelengths due to the influence of the nonlinear dispersion effect of dispersion. Subsequently, the emergence of the OWB generated by the four-wave mixing (FWM) was the dominant effect in the spectral broadening in these cases. The OWB starts appearing at 0.089 kW peak power at 0.98 μm and helps the spectrum broaden rapidly as the peak power continues to increase, OWB appears at shorter wavelengths. At a peak power of 0.133 kW (input pulse energy of 12 pJ), the spectrum extends from 0.81 μm to 1.919 μm with a relative power range of 5 dB. Figure 7(b) shows the temporal profile at different positions of the propagation length, respectively, with the spectrum growing along the #HF$_1$ fiber. In general, the time delay between different frequencies occurs earlier at shorter propagation when the input peak power is higher. Considered in each case, these values become larger with longer distances due to the difference in their group velocity components.

For the #HF$_2$ fiber, SC generation was analyzed with a pump wavelength of 1.55 μm, a pulse width of 110 fs and a fiber propagation length of 15 cm. #HF$_2$ fibers have pump wavelengths within the anomalous dispersion range, so soliton dynamics, e.g. SF, SSFS, play an important role in spectral broadening. As the process propagates further, the solitons continue to shift to longer wavelengths, resulting in a very large extension of the received spectrum towards the red-light region. Moreover, the DW component is generated by FWM and propagates without frequency shift.
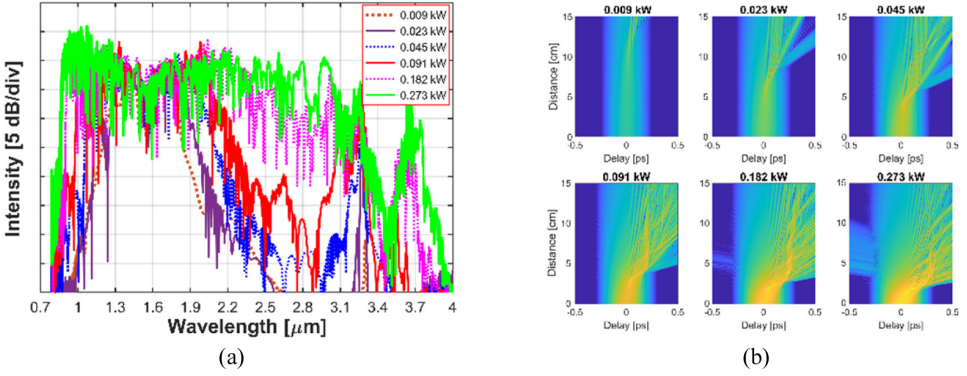
Fig. 8. (Color online) For #HF$_2$ fiber: (a) the output spectrum for various peak power pulses when using pump pulses with 1.55 μm pump wavelength and 110 fs duration and (b) the temporal profile at different positions of the propagation length, respectively, with the spectrum growing along the fiber.

Figure 8 shows the spectral evolution at different peak powers. At a peak power of 0.009 kW (input pulse energy of 1 pJ), the spectrum is smaller in this case because the SPM plays a major role in spectral broadening. Beyond a peak power of 0.009 kW, SF begins to appear, broadening the spectrum. As peak power increases, spectral width increases. However, for a peak power of 0.273 kW (input pulse energy of 30 pJ), the spectral width changes little compared to a peak power of 0.182 kW. This is explained by factors such as high dispersion slope in the short wavelength range, low nonlinear coefficient, and high loss in the long wavelength range. If the peak power equals 0.273 kW, the spectral bandwidth expands from 0.792 μm to 3.994 μm with a dynamic range of 5 dB.

We find that the SCG performance of our project is more optimal than that of the other tasks shown in Table 5. In particular, for anomalous dispersion regions, SC spectra in our work are the widest with the lowest peak power. In the all-normal dispersion mode, the proposed fiber can achieve the same bandwidth as the comparative claim, but with much lower peak power. In particular, the #HF$_1$ fiber has an extended spectrum from 0.81 μm to 1.919 μm with a peak power of 0.133 kW. Reference 28 has an extended spectrum from 0.64 μm to 1.7 μm, but consumes 93 times the peak power than our work. In Ref. 25 the author used a peak power of 55 kW and 413 times power in our study, but the spectral bands obtained are almost identical to the #HF$_1$ spectral bands. Moreover, the spectral range of our PCFs in the completely normal dispersion state is larger than that of the C$_7$H$_8$-filled PCFs in the previous study,[29,30] but the peak power used is lower. The all-normal dispersion optical fiber in Ref. 43 has a structure that varies with the air-hole diameter, as in our study, we obtain a spectral band approximately equal to the #HF$_1$ spectral band in this study, but using 3 times lower peak power. Besides, a nitrobenzene liquid-core PCF with eight elliptical air-holes in the innermost ring of the cladding is proposed in Ref. 13 with a peak power 7 times greater than that of #HF$_1$ fiber, but the obtained spectrum is approximate #HF$_1$ fiber from 1.3 μm to 2.8 μm. The above results

Table 5. The SC bandwidth of proposed PCFs in comparison with other silica-based PCF infiltration with liquid.

Liquid-core	Peak power (kW)	Pump wavelength (μm)	Fiber length (cm)	SC spectral range (μm)	Regime
#HF$_1$	0.133	1.56	1	0.81–1.919	All-normal
#HF$_2$	0.273	1.55	15	0.792–3.994	Anomalous
CCl$_4$[21]	62.5	1.03	20	0.85–1.25	All-normal
CHCl$_3$, #F$_1$[22]	2.5	1.03	10	0.6–1.26	All-normal
CHCl$_3$, #F$_2$[22]	2	1.03	10	0.6–1.4	Anomalous
C$_6$H$_5$NO$_2$, #F$_2$[23]	5.55	1.56	5.0	0.8–2.1	All-normal
C$_6$H$_5$NO$_2$, #F$_3$[23]	0.66	1.56	5.0	1.3–2.3	Anomalous
C$_6$H$_6$, #F$_1$[25]	55	1.56	1.0	0.7–2.0	All-normal
C$_6$H$_6$, #F$_3$[25]	37	1.56	1.0	0.6–3.5	Anomalous
C$_2$Cl$_4$, #F$_1$[26]	16.67	1.56	5.0	0.8–2.0	All-normal
C$_2$Cl$_4$, #F$_2$[26]	16.67	1.56	10	1.0–2.0	Anomalous
C$_2$Cl$_4$, #F$_3$[26]	20.83	1.03	10	0.7–2.4	Anomalous
C$_2$H$_4$Br$_2$, #F$_1$[28]	12.5	1.03	10	0.64–1.7	All-normal
C$_2$H$_4$Br$_2$, #F$_2$[28]	0.75	1.03	15	0.7–2.4	Anomalous
C$_7$H$_8$, #L0.3[29]	7.14	1.55	10	1.1–1.75	All-normal
C$_7$H$_8$, #L0.35[29]	6.67	1.55	10	1.0–1.75	Anomalous
C$_7$H$_8$[30]	25	1.03	10	0.95–1.1	All-normal
C$_7$H$_8$, #F$_1$[43]	0.45	1.064	1	0.642–1.592	All-normal
C$_7$H$_8$, #F$_2$[43]	0.55	1.55	10	0.911–2.496	Anomalous
C$_6$H$_5$NO$_2$[13]	1	1.81	5	1.3–2.8	All-normal

demonstrate the high potential of his proposed PCF for integrated and extensive SC generation systems.

5. Conclusion

In this paper, we designed a novel fused silica PCF with a $C_6H_5NO_2$-core. Hexagonal lattice PCFs are designed with a variable first ring air-holes diameter and a constant air-holes diameter of the remaining rings, the generated PCFs have minimal attenuation and the ability to control structural parameters to obtain optimal dispersion. The properties of the hexagonal lattice PCF are controlled by varying the structural parameters including the air-hole diameter in the first rings (d_1) and the lattice constant (Λ). Therefore, the PCFs in our work have flat dispersion, small effective mode area, high nonlinearity, and low attenuation for application for highly efficient SCG with much lower peak power than previously published. From the preliminary fiber design, we selected two fibers with optimized dispersion characteristics and analyzed SC generation in each.

The fiber #HF$_1$ operates in an all-normal dispersion regime with a lattice constant of $1.0\,\mu$m and a filling factor of 0.45. #HF$_1$ has flat dispersion, a small dispersion value of $-3.18\,\text{ps}\cdot\text{nm}^{-1}\cdot\text{km}^{-1}$, and a high nonlinear coefficient of $1497\,\text{W}^{-1}\cdot\text{km}^{-1}$ obtained at pump wavelength $1.56\,\mu$m. The main effect that dominates the SC spectrum broadening for #HF$_1$ fiber is SPM followed by OWB. The obtained SC spectrum extends from $0.81\,\mu$m to $1.919\,\mu$m and has a low peak

power of $0.133\,\text{kW}$ for ultra-short pulses spread within a $1\,\text{cm}$ propagation-long pass fiber.

On the other hand, the #HF$_2$ fiber exhibits anomalous dispersion with $d_1/\Lambda = 0.3$ and $\Lambda = 2.5\,\mu\text{m}$. The #HF$_2$ fiber has a low dispersion of $6.215\,\text{ps} \cdot \text{nm}^{-1} \cdot \text{km}^{-1}$, a low loss of $4.919\,\text{dB/cm}$, and a high nonlinear factor of $471\,\text{W}^{-1} \cdot \text{km}^{-1}$ at $1.55\,\mu\text{m}$ pump wavelength. Soliton dynamics including SF, SSFS, and DW are the main effects that make the SC spectrum of #HF$_2$ much broader than that of #HF$_1$ fiber. With a low peak power of $0.273\,\text{kW}$ and a pulse duration of $110\,\text{fs}$, the obtained HF$_2$ SC spectrum extends from $0.792\,\mu\text{m}$ to $3.994\,\mu\text{m}$ and propagates through a $15\,\text{cm}$ long fiber.

With such good advantages, our proposed fiber may become a new type of optical fiber suitable for low-peak power all-fiber laser systems in optical communication systems.

References

1. R. R. Alfano and S. L. Shapiro, *Phys. Rev. Lett.* **24**(11) (1970) 584.
2. G. Humbert, W. J. Wadsworth, S. G. Leon-Saval, J. C. Knight, T. A. Birks, P. St.J. Russell, M. J. Lederer, D. Kopf, K. Wiesauer, E. I. Breuer and D. Stifter, *Opt. Express* **14**(4) (2006) 1596.
3. N. M. Israelsen, C. R. Petersen, A. Barh, D. Jain, M. Jensen, G. Hannesschläger, P. Tidemand-Lichtenberg, C. Pedersen, A. Podoleanu and O. Bang, *Light Sci. Appl.* **8**(1) (2019) 11.
4. J. T. Woodward, A. W. Smith, C. A. Jenkins, C. Lin, S. W. Brown and K. R. Lykke, *Metrologia* **46**(4) (2009) S277.
5. D. R. Carlson, D. D. Hickstein, A. Lind, J. B. Olson, R. W. Fox, R. C. Brown, A. D. Ludlow, Q. Li, D. Westly, H. Leopardi, T. M. Fortier, K. Srinivasan, S. A. Diddams and S. B. Papp, *Phys. Rev. Appl.* **8**(1) (2017) 014027.
6. T. Fortier and E. Baumann, *Commun. Phys.* **2**(1) (2019) 153.
7. L. C. Van, L. M. Van and Q. H. Quang, *Commun. Phys.* **18**(4) (2008) 255.
8. L. C. Van, L. M. Van, K. D. Xuan, S. V. Ngoc, T. N. T. Thanh and Q. H. Quang, *Commun. Phys.* **18**(2) (2008) 119.
9. L. C. Van and K. D. Xuan, *Commun. Phys.* **17**(4) (2007) 227.
10. L. C. Van, T. N. Thi, T. L. T. Bao, D. H. Trong, N. V. T. Minh, H. V. Le and V. T. Hoang, *Photonics Nanostruct. — Fundamentals Applic.* **48** (2022) 100986.
11. M. R. Karim, H. Ahmad and B. M. A. Rahman, *J. Opt. Fiber Technol.* **45** (2018) 255.
12. M. R. Karim, H. Ahmad and B. M. A. Rahman, *IEEE Photonics Technol. Lett.* **29**(21) (2017) 1792.
13. J. Wen, B. Liang, W. Qin, W. Sun, C. He and K. Xiong, *Opt. Quantum Electron.* **54** (2022) 817.
14. V. Devika, M. S. M. Rajan and M. Sharma, *Opt. Quantum Electron.* **54** (2022) 858.
15. V. Devika, M. S. M. Rajan, H. Thenmozhi and A. Sharafali, *J. Opt.* **54** (2022).
16. A. Nair, C. S. Boopathi, M. Jayaraju and M. S. M. Rajan, *Optik* **179** (2019) 718.
17. D. Churin, T. N. Nguyen, K. Kieu, R. A. Norwood and N. Peyghambarian, *Opt. Mater. Express* **3** (2013) 1358.
18. S. Junaid, J. Bierlich, A. Hartung, T. Meyer, M. Chemnitz and M. A. Schmidt, *Opt. Express* **29**(13) (2021) 19891.

19. Q. H. Dinh, J. Pniewski, H. L. Van, A. Ramaniuk, V. C. Long, K. Borzycki, K. D. Xuan, M. Klimczak and R. Buczynski, *Appl. Opt.* **57**(14) (2018) 3738.
20. V. T. Hoang, R. Kasztelanic, G. Stępniewski, K. D. Xuan, V. C. Long, M. Trippenbach, M. Klimczak, R. Buczynski and J. Pniewski, *Appl. Opt.* **59**(12) (2020) 3720.
21. V. T. Hoang, R. Kasztelanic, A. Filipkowski, G. Stępniewski, D. Pysz, M. Klimczak, S. Ertman, V. C. Long, T. R. Woliǹski, M. Trippenbach, K. D. Xuan, M. Sṁietana and R. Buczyǹski, *Opt. Mater. Express* **9**(5) (2019) 2264.
22. L. C. Van, T. V. Hoang, V. C. Long, K. Borzycki, K. D. Xuan, V. T. Quoc, M. Trippenbach, R. Buczyński and J. Pniewski, *Laser Phys.* **29**(7) (2019) 075107.
23. L. C. Van, T. V. Hoang, V. C. Long, K. Borzycki, K. D. Xuan, V. T. Quoc, M. Trippenbach, R. Buczyński and J. Pniewski, *Laser Phys.* **30**(3) (2020) 035105.
24. L. C. Van, T. N. Thi, D. H. Trong, B. T. L. Tran, N. V. T. Minh, T. D. Van, T. L. Canh, Q. H. Dinh and K. D. Quoc, *Opt. Quantum Electron.* **54**(5) (2022).
25. L. C. Van, V. T. Hoang, V. C. Long, K. Borzycki, K. D. Xuan, V. T. Quoc, M. Trippenbach, R. Buczynski and J. Pniewski, *Opt. Eng.* **60**(11) (2021) 116109.
26. H. V. Le, V. T. Hoang, H. T. Nguyen, V. C. Long, R. Buczynski and R. Kasztelanic, *Opt. Quantum Electron.* **53** (2021) 187.
27. L. C. Van, H. V. Le, N. D. Nguyen, N. V. T. Minh, Q. H. Dinh, V. T. Hoang, T. N. Thi and B. C. Van, *Laser Phys.* **32** (2022) 055102.
28. H. V. Le, V. T. Hoang, Q. D. Ho, H. T. Nguyen, N. V. T. Minh, M. Klimxzak, R. Buczynski and R. Kasztelanic, *Appl. Opt.* **60**(24) (2021) 7268.
29. L. C. Van, A. Anuszkiewicz, A. Ramaniuk, R. Kasztelanic, K. D. Xuan, V. C. Long, M. Trippenbach and R. Buczynski, *J. Opt.* **19**(12) (2017) 125604.
30. V. T. Hoang, R. Kasztelanic, A. Anuszkiewicz, G. Stepniewski, A. Filipkowski, S. Ertman, D. Pysz, T. Wolinski, K. D. Xuan, M. Klimczak and R. Buczynski, *Opt. Mater. Express* **8**(11) (2018) 3568.
31. K. Saitoh, M. Koshiba, T. Hasegawa and E. Sasaoka, *Opt. Express* **11** (2003) 843.
32. Lumerical Solutions Inc., Mode solution, https:www.lumerical.com/tcad-products/mode/.
33. Y. Xu, X. Chen and Y. Zhu, *Sensors* **8** (2008) 1872.
34. M. Vieweg, T. Gissibl, S. Pricking, B. T. Kuhlmey, D. C. Wu, B. J. Eggleton and H. Giessen, *Opt. Express* **18**(24) (2010) 25232.
35. R. Zhang, J. Teipel and H. Giessen, *Opt. Express* **14**(15) (2006) 6800.
36. Z. Zhu and T. G. Brown, *Opt. Express* **10** (2002) 853.
37. D. Pysz, I. Kujawa, R. St□pień, M. Klimczak, A. Filipkowski, M. Franczyk, L. Kociszewski, J. Buźniak, K. Haraśny and R. Buczyński, *Bull. Pol. Acad. Sci.: Tech. Sci.* **62**(4) (2014) 667.
38. S. Kedenburg, M. Vieweg, T. Gissibl and H. Giessen, *Opt. Mater. Express* **2**(11) (2012) 1588.
39. C. Z. Tan, *J. Non-Cryst. Solids* **223**(1–2) (1998) 158.
40. G. P. Agrawal, *Nonlinear Fiber Optics*, Chapter 2, 5th edn. (Academic Press, Elsevier, 2013).
41. F. Koohi-Kamalia, M. Ebnali-Heidarib and M. K. Moravvej-Farshic, *Int. J. Opt. Photonics* **6**(2) (2012).
42. R. Raei, M. Ebnali-Heidari and H. Saghaei, *J. Opt. Soc. Am. B* **35**(2) (2018) 323.
43. T. N. Thi, D. H. Trong, B. T. L. Tran, T. D. Van and L. C. Van, *J. Opt.* **51** (2022) 678.